Chapter 10
Stokes Imaging: Mapping the Accretion Region(s) in Magnetic Cataclysmic Variables

Stephen B. Potter

10.1 Introduction

Magnetic cataclysmic variables (mCVs) are interacting binaries in which material overflows the Roche lobe of a red-dwarf secondary star and is accreted onto a magnetic white dwarf star (Fig. 10.1). See [11] and [42] for a review of mCVs. A subclass of mCVs, known as polars, have a sufficiently strong white dwarf magnetic field that the system is locked into synchronous rotation and prevents an accretion disc from forming.

The accretion material initially leaves the inner Lagrange point and follows a ballistic trajectory. At some distance from the white dwarf, the stress of the white dwarf magnetic field overwhelms the ram pressure of the ballistic stream and its flow becomes directed by the magnetic-field lines. The magnetically confined supersonic flow eventually becomes subsonic at a shock front at some height above the white dwarf surface.

The shock, which typically has a temperature of $\sim$10–50 keV, heats and ionizes the accreting material. The shocked-heated material cools as it settles onto the white dwarf surface, forming a stratified (in density and temperature) relaxation region. Further details of the standard shock model can be found in the following review by Wu and references therein [48].

The main radiative-transport processes, in the post-shock region, are bremsstrahlung and cyclotron cooling. Bremsstrahlung radiation is emitted in the keV X-ray band, and the post-shock region is optically thin to the bremsstrahlung X-rays. Cyclotron radiation is emitted in the optical and IR bands, and it is strongly polarised (Fig. 10.2). The post-shock region is opaque to the optical/IR cyclotron emission at low frequencies but is transparent in the blue/UV frequencies.

S.B. Potter (✉)
South African Astronomical Observatory, Cape Town, South Africa
e-mail: sbp@saao.ac.za

H.M.J. Boffin et al. (eds.), *Astronomy at High Angular Resolution*, Astrophysics and Space Science Library 439, DOI 10.1007/978-3-319-39739-9_10

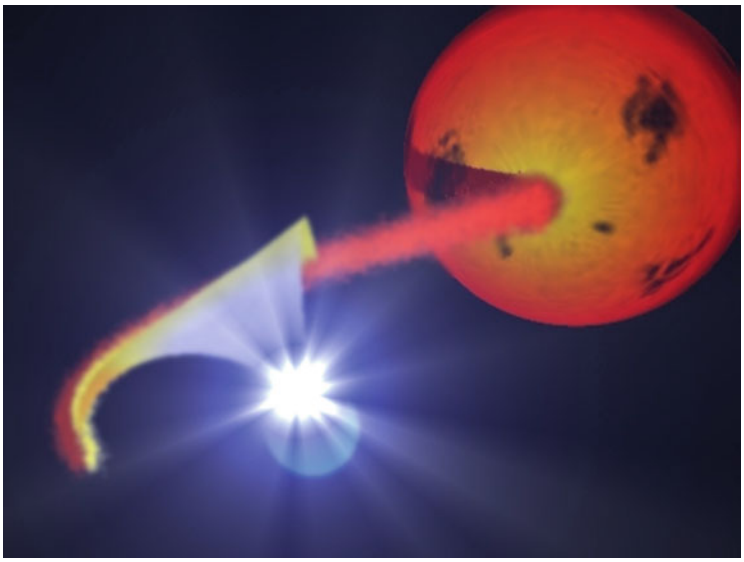

Fig. 10.1 A schematic of a polar, a sub-class of the magnetic Cataclysmic Variables. The *red dwarf* secondary star, the ballistic stream, the magnetic accretion curtain and the bright accretion region on the surface of the *white dwarf* are shown here

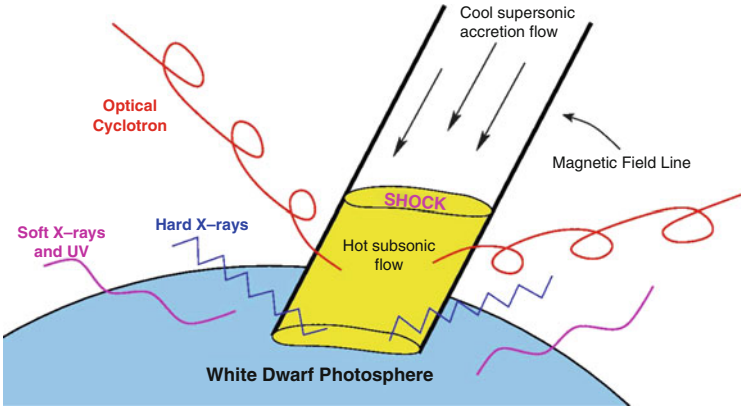

Fig. 10.2 A schematic of the accretion region on the surface of the *white dwarf* highlighting the emission mechanisms

10.2 Polarisation Modelling

Over the course of a binary orbit (typically a few hours) the polarised optical emission is observed to be highly variable. This is because the cyclotron emission from the shock is highly dependent on viewing angle. For example, when our

viewing angle is such that we are looking down towards the top of the shock, effectively parallel to the magentic field lines, an increase in the amount of circularly polarised flux is observed. When the viewing angle changes to being perpendicular to the magnetic field lines, effectively viewing the side of the shock, an increase in linear polarised flux is observed. The actual morphology of the orbitally phase-resolved polarised variations will depend on the location, size and shape of the localised cyclotron emission region(s) on the surface of the white dwarf.

With appropriate modelling of the polarised cyclotron emission, the location, size and shape of the localised cyclotron emission region(s) can be reconstructed, (e.g., [2, 6–8, 10, 15, 25–28, 31, 34, 40, 44, 45, 53]). At the core of these studies are the cyclotron-opacity and radiative-transfer calculations. Two formulations are commonly used in the calculations: the decomposed normal-mode formulation (e.g., [7]), which is valid in the limit of large Faraday rotation; and the more general 4-Stoke formulation (e.g., [25, 26]).

Meggitt & Wickramashinghe provided tables of the results of their calculations assuming that the heated shock region can be represented as a simple hemisphere of constant temperature and density (Fig. 10.3 and [25, 26]). The tables provide the polarised Stokes parameters as a function of viewing angle from which one could then produce model phase-resolved polarised light curves. They calculated multiple tables, each representing shocks of different magnetic field strengths, temperatures, densities and a plasma parameter Λ (representing the electron density and characteristic size of the emission region).

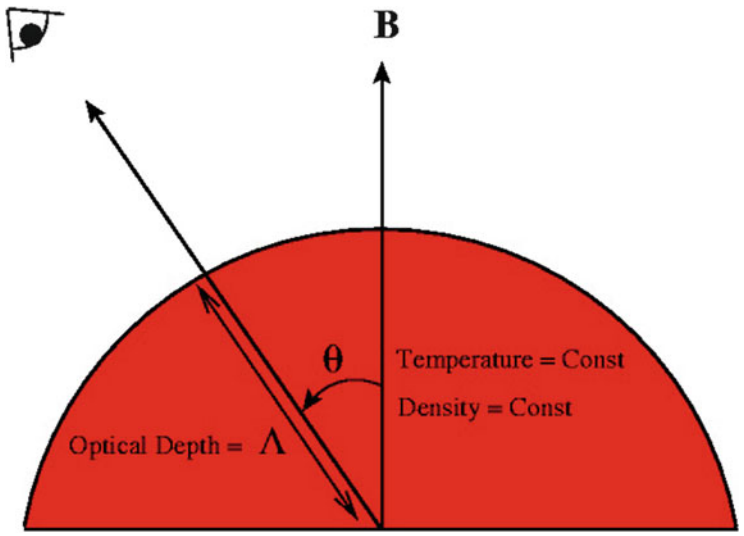

Fig. 10.3 A schematic of a *hemisphere* used in performing the radiative transfer calculations

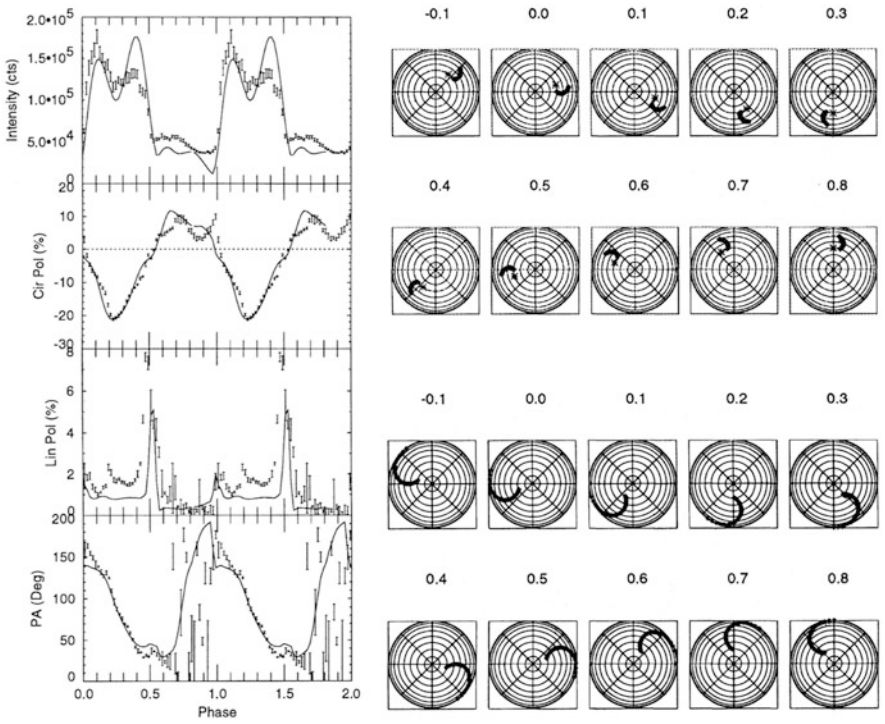

Fig. 10.4 *Left*: Orbitally phase-resolved optical photo-polarimetric observations of the polar REJ1844-74, with model over-plotted. Intensity, circular and linear polarisation and position angle can be seen from top to bottom. *Right*: Views of the upper and lower accretion arcs used to produce the model polarisation (Reproduced with permission from Ramsay et al. [34])

Cyclotron emission regions of arbitrary shapes, sizes and locations could then be constructed by using several such hemispheres. Figure 10.4 shows such an example taken from Ramsay et al. [34]. They considered several accretion regions of differing extents on the surface of the white dwarf such that a crude fit to the light curve was obtained. The magnetic field strength, plasma parameter, the inclination, and the colatitude of the magnetic axis was then modified until a solution was found that fitted all three polarisation curves relatively well. The temperature was taken to be 10 keV. The accuracy of the fit is remarkably good with all the major features in the light curves being well reproduced. However, not all of the detailed features could be modelled. They found that two model emission regions represented as long, thin arcs gave the best fits (see Fig. 10.4). Several authors have successfully used similar modelling techniques to those noted above in order to reconstruct the shape, size and location of the cyclotron emission regions and have generally found that long thin arcs best fit the observations.

10.3 Stokes Imaging

Despite the success of modelling the cyclotron emission regions, it was clear that the approach was largely by trial and error until the model gave a good fit to the observations. A more objective technique was required in order to take the modelling procedure to the next step and to eliminate any initial biases the astronomer may have.

Stokes imaging as described by Potter, Hakala & Cropper is such a technique [31]. The trial and error approach has been replaced with a Genetic Algorithm (GA) which optimises the model to the observations.

The GA works by first generating a set of random solutions. Each solution consists of a large number of hemispheres placed randomly over the surface of the white dwarf. The "fitness" of each solution is then calculated using:

$$F(p) = \chi^2 + \lambda \sum_i ||\nabla p_i||^2;$$

where χ^2 is the χ^2-fit to the observations, λ is a Lagrangian multiplier, p_i is a single emission element on the surface of the white dwarf, $||\nabla p_i||$ is the mean gradient of the number of emission points at point i.

Minimising this with a suitable choice of the Lagrangian multiplier, λ, will produce the maximum entropy solution of the distribution of emission points. The GA then breeds all the solutions by using a type of natural selection procedure; the "fittest" solutions have a higher probability of being selected for breeding. Eventually the improvement in fitness of the GA solutions starts to level out and a more analytical approach is used to improve the fit further. The technique is best demonstrated through the example test case displayed in Fig. 10.5. Figure 10.5a shows a model white dwarf with two arc-like emission regions. The corresponding model light curves are shown in Fig. 10.5b. After several generations the solutions start to converge. One such solution is displayed in Fig. 10.5c which has clearly started to resemble the input image. At this stage the GA approach becomes inefficient at progressing further. A more analytical technique now takes over which effectively "cleans up" the image to give the final solution in Fig. 10.5d. The model prediction is overplotted on the input light curve in Fig. 10.5b. See [31] for details and more test cases.

Stokes imaging has been applied to several mCVs, each with differing morphologies and quality of observations. These include CP Tuc [35], ST Lmi [28], V347 Pav [30], RXJ2115 [36], QS Tel [37], V834 Cen [32], HU Aqr [16] and CTCVJ1928-5001 [29].

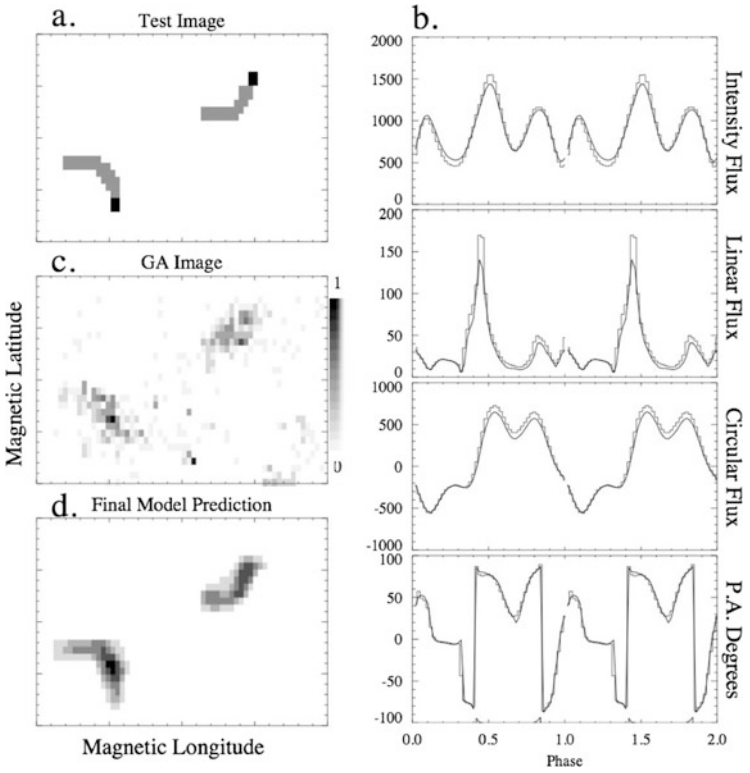

Fig. 10.5 Model white dwarf with two arc-like emission regions: (**a**) the input test image; (**b**) the input test data and final model solution; (**c**) the GA optimised image; (**d**) the final optimised image

10.4 Photo-polarimetric Observations of the Eclipsing Polar CTCV J1928-5001

Figure 10.6 shows polarimetric observations of the eclipsing polar CTCV J1928-5001 taken in August 2003 on the 1.9 m of the South African Astronomical Observatory using the UCT polarimeter [10]. These results were extracted from work published in [29]. The photometry and polarimetry are modulated on a period of $\sim$101 min. Circular polarisation variations are seen from approximately -8 to 12 % in the unfiltered observations. Two linear polarised pulses are detected at orbital phases coinciding with the reversals in the circular polarisation.

Figure 10.6 shows the model fit from Stokes imaging that has reproduced the main polarisation morphology and predicted two emission regions. The predicted upper emission region is also displayed in Fig. 10.6 for two different assumed system inclinations. Simple, single particle ballistic and magnetic trajectories were also calculated and over-plotted. As can be seen from Fig. 10.6, the magnetic footprints were found to have the best overlap with the emission region for

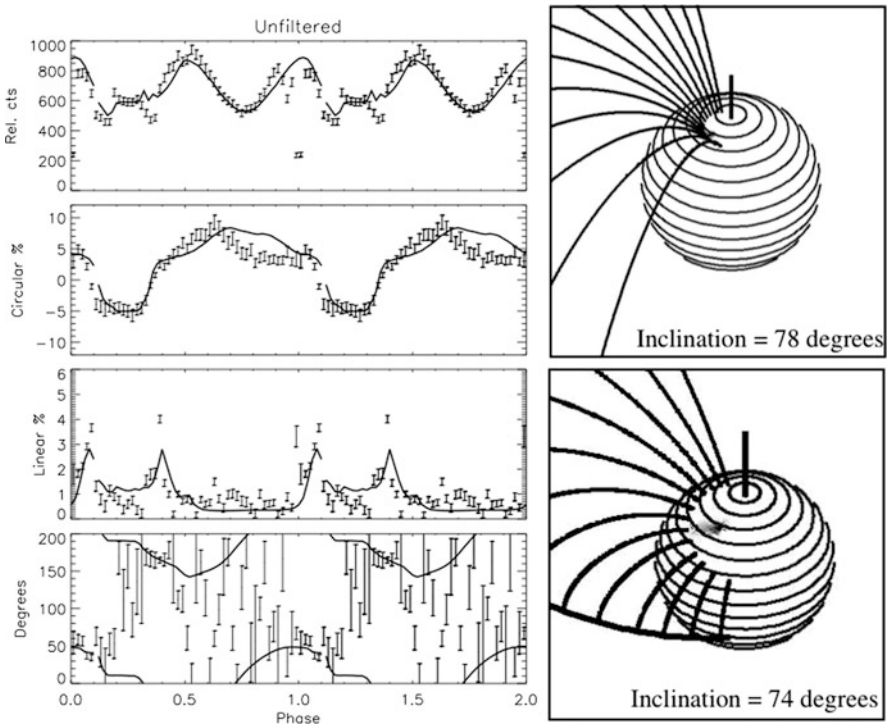

Fig. 10.6 *Left*: folded, unfiltered photo-polarimetric observations and model fit of the eclipsing polar CTCVJ1928-5001. *Right*: the location of the accretion region on the surface of the white dwarf for different model solutions. Magnetic trajectories also shown (Reproduced with permission from Potter, Augesteijn & Tappert [29])

inclinations ∼78°. Reassuringly such an inclination is in agreement with the implied mass ratios and primary masses for CVs with similar orbital periods [41] and is consistent with the range of inclinations estimated from using the eclipse length [17]. The location of the lower accretion region (not shown) does not overlap with the magnetic footprints so well. The authors concluded that this is an indication that the magnetic field of the white dwarf is not a simple dipole but is at least an offset dipole field (see [29] for further details).

10.5 Future Work: Stratified Accretion Shocks

The work discussed so far relied on simple emission regions with constant density, temperature and magnetic field. The geometry was assumed to be either an infinitely small hemisphere with finite opacity (e.g., [25, 26]) or a semi-infinite slab (e.g., [2, 3, 7]). However, it was first suggested by Ferrario, Bailey & Wickramasinghe

[13], that the single temperature models are insufficient to reproduce the cyclotron spectrum and indeed multi-waveband polarimetric light curves.

Some later calculations included the spatial variations in the temperature, density and magnetic field and considered more complicated geometries, e.g., cylinders, for the emission region. These inhomogeneous models (e.g., [45, 49–51]) were generally parametric, with the temperature and density variations treated in an ad hoc manner. More realistic settings were considered in the next generation of inhomogeneous models. For example, 3-D emission regions confined by a dipole magnetic field [4–6], or ridge-like emission regions [53]. Eventually, models were used in which the density and temperature structures of the emission regions were determined by hydrodynamic calculations [14, 46, 53, 54].

These hydrodynamic calculations, performed in parallel to the radiative-transfer calculations, were carried out to model the temperature and density structures of the emission regions properly. The models evolved from one-temperature hydrodynamic models with bremsstrahlung (or a single) cooling [1, 9, 18]; one-temperature models with multiple cooling processes (e.g., [12, 47, 52]); to the full-fledged two-temperature models which include effects due to unequal electron and ion temperature [14, 20, 21, 38, 39, 46]. Other effects, such as variation of the gravity along the flow, were also considered (e.g., [12, 19]). Cropper et al. [12] demonstrated that gravity has substantial effects on the hydrodynamics of the flow. When a gravity term is included in the hydrodynamic calculations, it increases the thickness of the shock-heated region but reduces the shock temperature. The X-rays from the resulting post-shock region are therefore softer than when the gravity term is omitted. Thus, if gravity effects are neglected, white dwarf masses will be overestimated when using X-ray spectra to determine the white dwarf masses of mCVs [33].

Figure 10.7 shows an example of hydrodynamic calculations for three different white dwarf masses. In each case (white dwarf masses of 0.5, 0.85 and 1.2 $M_{\odot}$) the vertical temperature structure is plotted as a function of height for different accretion rates. As can be seen, the temperature-height relation is strongly dependent on the white dwarf mass. Furthermore, there is also a strong dependence on magnetic field strength (not shown).

We performed the radiative transfer calculations in order to derive the intensities and polarisations from structured emission regions, constructed using the hydrodynamic model. The aim being to produce more realistic grids of spectra and polarisations for modelling the polarised optical/IR radiation from mCVs such as Stokes imaging.

We considered ray-tracing calculations along the lines-of-sight starting from designated emitting points to an observer at infinity. The emission region is divided into strata, each with homogeneous temperatures and densities. The temperature and density of each stratum are obtained by discretising the temperature and density structures of the emission region obtained from the hydrodynamic calculations.

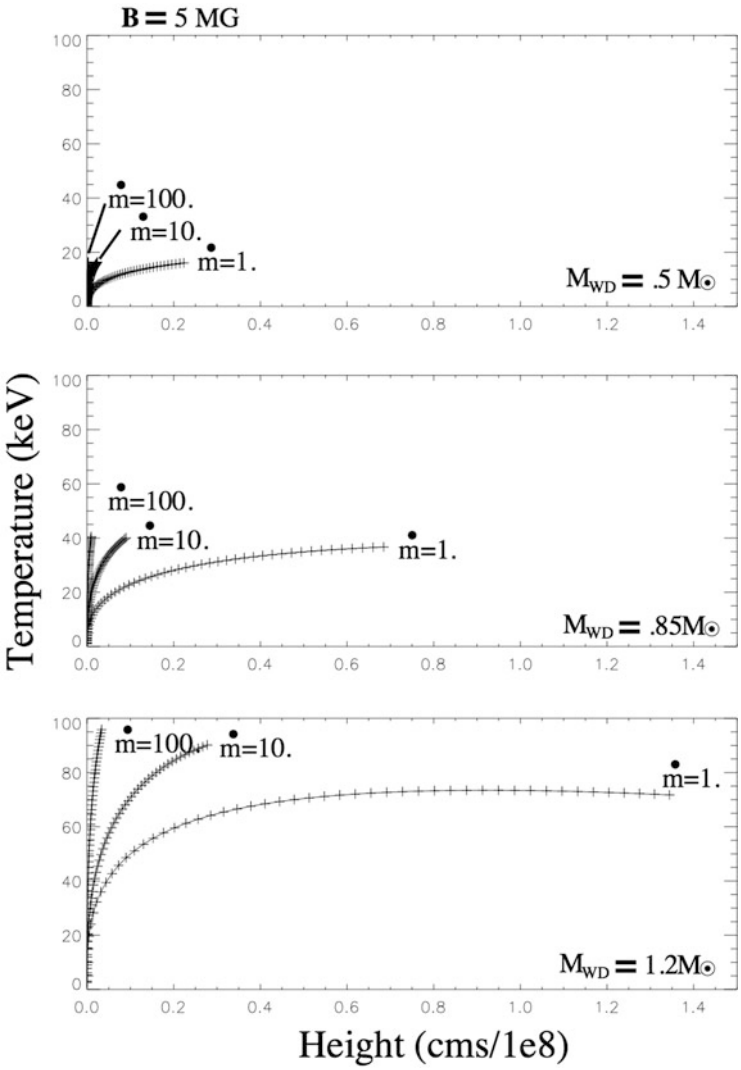

Fig. 10.7 Temperature profiles in the post-shock regions for white dwarf mass of 0.5, 0.85 and 1.2 $M_{\odot}$. In each panel, three cases with the specific accretion rate of 1, 10 and 100 g cm^{-2} s^{-1} are shown. The magnetic field strength of the white dwarf is fixed at 5 MG

We lay a rectangular grid at the bottom of each stratum and consider rays starting from emitting points located on the grid (Fig. 10.8). Each ray is independent but its intensity and polarisations are modified by the line-of-sight materials in the strata above.

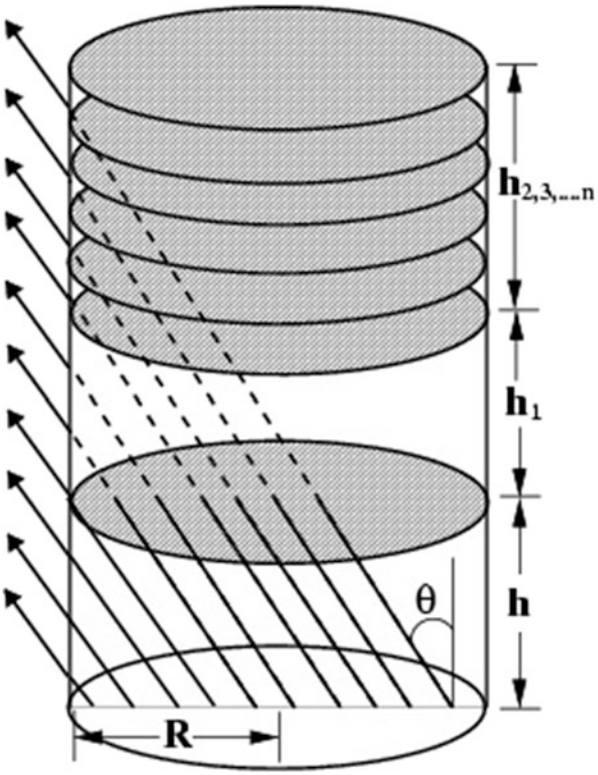

Fig. 10.8 An illustration of the ray-tracing algorithm used in the polarisation radiative-transfer calculations. The *cylindrical* emission region is divided into strata of equal thickness and cross-section radius. The cylinder is embedded in a magnetic field parallel to the symmetry axis. Shown are the light paths of emission from one of the strata for a particular viewing angle. The Stokes parameters are calculated for each ray and the resultant Stokes parameters are the sum of all rays

Figure 10.9 shows an extract of the grid corresponding to the structured shocks shown in Fig. 10.7. These grids demonstrate the future potential of Stokes imaging to derive fundamental parameters of mCVs, such as white dwarf mass, magnetic field strength and the temperature and density profile of the shock(s). For example, simply comparing the intensity grids only (top row, from left to right) one can see that there is not only a peak intensity wavelength dependence on the white dwarf mass (decreasing from $\sim$0.61 to $\sim$0.38 microns for 0.5 to 1.2 $M_{\odot}$) but also a significant spectral morphology change, i.e., the lower mass white dwarf shows significant cyclotron humps in the spectra which are not so apparent in the higher mass white dwarf. The circular and linear polarisation show significantly more morphological dependence on white dwarf mass as a function of viewing angle. Indeed, Fig. 10.9 is only an extract from the grid of calculations. The other dimensions of the grid include magnetic field strength, specific accretion rate and radius of the accretion column. Combined with orbitally phase-resolved spectro-

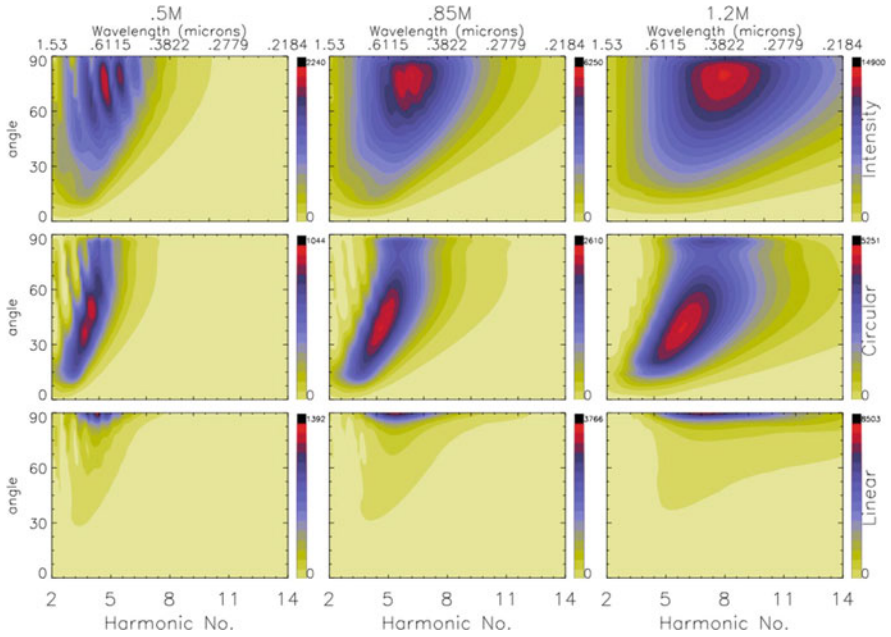

Fig. 10.9 The cyclotron intensity and polarisations from a structured emission region for white dwarf masses of 0.5, 0.85 and 1.2 $M_{\odot}$ (left to right columns respectively). The accretion rate is $\dot{m} = 1.0\,\mathrm{g\,cm^{-2}\,s^{-1}}$, the magnetic field, $B = 35\,\mathrm{MG}$, and the radius of the accretion column, $R = 10^4\,\mathrm{cm}$

polarimetry, we anticipate these grids will be a powerful diagnostic for deriving the fundamental parameters of the white dwarfs in mCVs.

10.6 Future Work: Multi-tomography

The true benefit of Stokes imaging comes when combined with other tomographic techniques (e.g., [32]). Stokes imaging was combined with the analysis of spectroscopic observations using the Doppler tomography and Roche tomography techniques of Marsh & Horne and Watson & Dhillon [23, 43]. Up to then, all three techniques had been used separately to investigate the geometry and accretion dynamics in cataclysmic variables. For the first time, Potter et al. [32] applied all three techniques to simultaneous polarimetric and spectroscopic observations for a single system (V834 Cen). This allowed them to compare and test each of the techniques against each other and hence to derive a better understanding of the geometry, dynamics and system parameters. Figures 10.10 and 10.11 show the results.

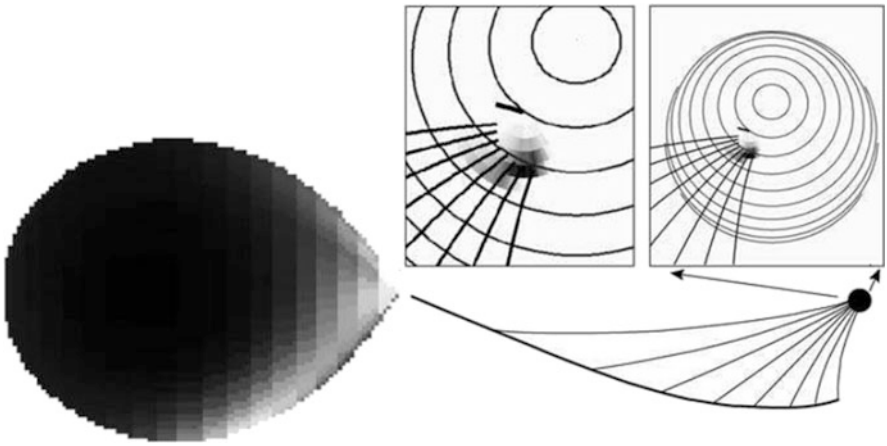

Fig. 10.10 The derived Stokes image (*inserts*) and Roche tomogram of the secondary star. Ballistic and magnetic trajectories are over-plotted and also shown over-plotted on the Doppler tomogram in Fig. 10.11

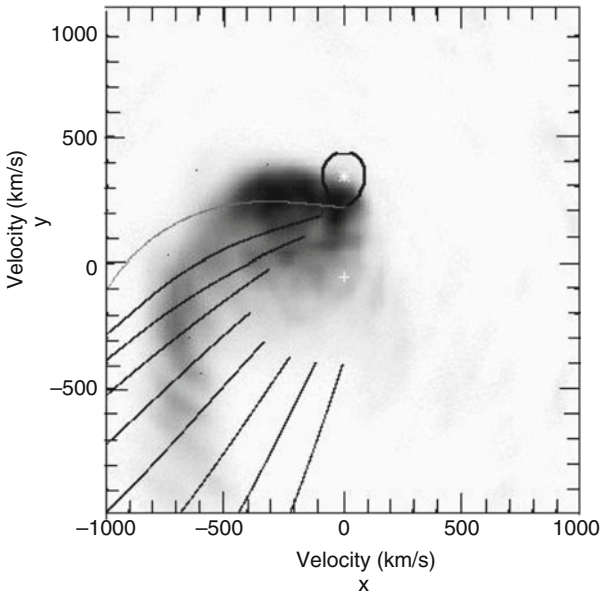

Fig. 10.11 Doppler tomogram of the HeII emission line form V834 Cen. The same ballistic and magnetic trajectories have been over-plotted as in Fig. 10.10

Stokes imaging predicted a single emission region, visible for the whole orbit, to be responsible for the observed polarised variations. The location of the region on the white dwarf was found to be consistent with EUV observations [24]. Both analyses placed the main emission region approximately more than 40° and up to

70° in azimuth from the line of centres of the two stars. The Doppler tomographic analysis showed several components associated with the secondary star, the ballistic stream and parts of the magnetically confined stream. Magnetic Doppler trajectories were also calculated and shown to be generally coincident with the magnetic signatures found in the Doppler maps and, furthermore, the footprints of the magnetic field lines on the surface of the white dwarf were shown to be coincident with the prediction for the location of the cyclotron emission region from Stokes imaging. Roche tomography of the narrow component seen in the He II 4686 Å emission line revealed two asymmetries in the emission distribution on the Roche surface of the secondary. Namely, there was generally more emission on the inner surface and also on the leading face of the secondary. They argued that this was consistent with irradiation of the secondary and not only supported by the Doppler tomogram, but also by the Stokes imaging results, which showed that most of the accreting material comes along field lines that intersect the later parts of the ballistic stream.

We next plan to exploit recent advances made in Doppler tomography, namely the inside-out variant as described by Kotze, Potter & McBride [22]. An example of this technique is shown in Fig. 10.12, which displays a He II Doppler tomogram of the polar UZ For together with its inside-out Doppler tomogram.

The inside-out technique effectively reverses the velocity axis to create an inside-out Doppler coordinate framework with the intent to expose/enhance emission details that are overly compacted/washed-out in the standard Doppler framework. The technique appears to be especially effective at separating the velocity components in polars. Figure 10.12 clearly shows how emission from the secondary, the

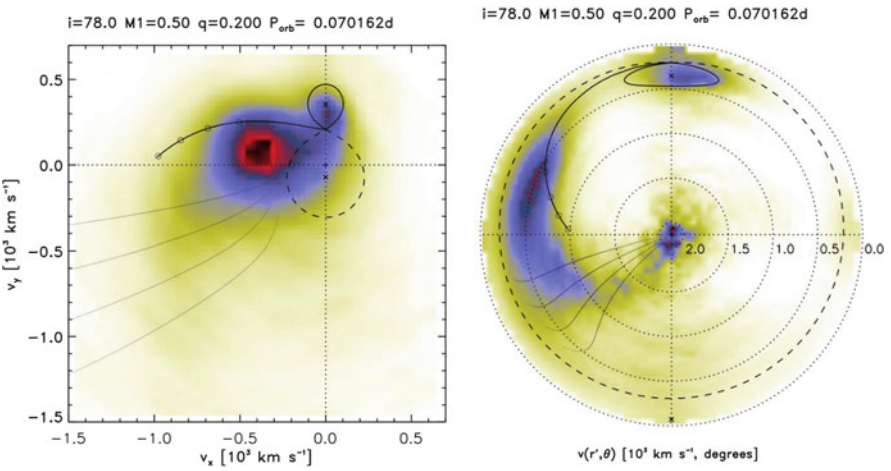

Fig. 10.12 *Left*: A Doppler tomogram of the HeII emission from the polar UZ For. *Right*: An inside-out Doppler tomogram of the same data set. In both cases the same model ballistic and magnetic accretion curtains are over-plotted as well as the roche lobes of the secondary and primary stars

ballistic and magnetic streams are easier to distinguish from each other compared to the normal tomogram. In particular the high-velocity components of the emission line, which is washed out towards the lower left quadrant of the normal Doppler map, becomes more compact and enhanced in the inside-out framework. Combining this technique with the other tomographic techniques, described above, will be our next step.

References

1. Aizu, K.: X-Ray emission region of a white dwarf with accretion. Progr. Theor. Phys. **49**, 1184 (1973)
2. Barrett, P.E., Chanmugam, G.: Polarized radiation from hot plasmas and applications to AM Herculis binaries. II – effect of collisions and Thomson scattering. ApJ **278**, 298 (1984)
3. Barrett, P.E., Chanmugam, G.: Cyclotron lines in accreting magnetic white dwarfs with an application to VV Puppis. ApJ **298**, 743 (1985)
4. Canalle, J.B.G., Opher, R.: The cyclotron spectrum of VV Puppis. A&A **189**, 325 (1988)
5. Canalle, J.B.G., Opher, R.: Cyclotron spectrum from a dipole magnetic field accretion column. A&A **219**, 334 (1989)
6. Canalle, J.B.G., Opher, R.: The accretion column of DQ Herculis binaries. A&A **251**, 474 (1991)
7. Chanmugam, G., Dulk, G.A.: Polarized radiation from hot plasmas and applications to AM Herculis binaries. ApJ **244**, 569 (1981)
8. Chanmugam, G., Frank, J., King, A.R., et al.: The magnetic field of the intermediate polar BG Canis Minoris. ApJ **350**, L13 (1990)
9. Chevalier, R.A., Imamura, J.N.: Linear analysis of an oscillatory instability of radiative shock waves. ApJ **261**, 543 (1982)
10. Cropper, M.S.: Simultaneous linear and circular polarimetry of EF ERI. MNRAS **212**, 709 (1985)
11. Cropper, M.S.: The polars. Space Sci. Rev. **54**, 195 (1990)
12. Cropper, M.S., Wu, K., Ramsay, G., et al.: Effects of gravity on the structure of post-shock accretion flows in magnetic cataclysmic variables. MNRAS **306**, 684 (1999)
13. Ferrario, L., Bailey, J., Wickramasinghe, D.T.: Detection of cyclotron emission features in the infrared spectrum of ST LMi. MNRAS **262**, 285 (1993)
14. Fischer, A., Beuermann, K.: Accretion physics of AM Herculis binaries. I. Results from one-dimensional stationary radiation hydrodynamics. A&A **373**, 211 (2001)
15. Frank, J., Chanmugam, G.: Polarized radiation from magnetic accretion rings. ApJ **365**, 660 (1990)
16. Harrop-Allin, M.K., Potter, S.B., Cropper, M.: Indirect imaging of the accretion stream in eclipsing polars – III. HU Aquarii low state. MNRAS **326**, 788 (2001)
17. Horne K.: Images of accretion discs. I – the eclipse mapping method. MNRAS **213**, 129 (1985)
18. Hoshi, R.: X-Ray emission from white dwarfs in close binary systems. Progr. Theor. Phys. **49**, 776 (1973)
19. Imamura, J.N., Durisen, R.H.: X-ray spectra and light curves of accreting magnetic degenerate dwarfs. ApJ **268**, 291 (1983)
20. Imamura, J.N., Aboasha, A., Wolff, M.T., et al.: The stability properties of two-temperature white dwarf radiative shock waves. ApJ **458**, 327 (1996)
21. Imamura, J.N., Durisen, R.H., Lamb, D.Q., et al.: X-ray and ultraviolet radiation from accreting white dwarfs. IV – two-temperature treatment with electron thermal conduction. ApJ **378**, 665 (1987)

22. Kotze, E., Potter, S., McBride, V.: Exploring inside-out Doppler tomography: non-magnetic cataclysmic variables. A&A **579**, A77 (2015)
23. Marsh, T.R., Horne, K.: Images of accretion discs. II – doppler tomography. MNRAS **235**, 269 (1988)
24. Mauche, C.W.: Extreme ultraviolet explorer phase-resolved spectroscopy of V834 Centauri. ApJ **578**, 439 (2002)
25. Meggitt, S.M.A., Wickramasinghe, D.T.: The polarization properties of magnetic accretion columns. MNRAS **198**, 71 (1982)
26. Meggitt, S.M.A., Wickramasinghe, D.T.: An analysis of the cyclotron spectrum and polarization properties of VV puppis. MNRAS **198**, 975 (1982)
27. Piirola, V., Coyne, G.V., Takalo, S.J.L., et al.: UBVRI polarimetry of AM Herculis-type binaries. 5: the asynchronous (?) polar BY Camelopardalis (H0538+608). A&A **283**, 163 (1994)
28. Potter, S.B.: Stokes imaging of the AM Her system ST LMi. MNRAS **314**, 672 (2000)
29. Potter, S.B., Augusteijn, T., Tappert, C.: Photopolarimetric observations of the new eclipsing polar CTCVJ1928 – 5001. MNRAS **364**, 565 (2005)
30. Potter, S.B., Cropper, M., Hakala, P.J.: Stokes imaging of the accretion region in magnetic cataclysmic variables – II. V347 Pav. MNRAS **315**, 423 (2000)
31. Potter, S.B., Hakala, P.J., Cropper, M.: 'Stokes imaging' of the accretion region in magnetic cataclysmic variables – I. conception and realization. MNRAS **297**, 1261 (1998)
32. Potter, S.B., Romero-Colmenero, E., Watson, C., et al.: Stokes imaging, doppler mapping and Roche tomography of the AM Herculis system V834 Cen. MNRAS **348**, 316 (2004)
33. Ramsay, G.: Determining the mass of the accreting white dwarf in magnetic cataclysmic variables using RXTE data. MNRAS **314**, 403 (2000)
34. Ramsay, G., Cropper, M., Wu, K., et al.: Optical polarization and X-ray data on the AM HER star RE J1844-74. MNRAS **282**, 726 (1996)
35. Ramsay, G., Potter, S.B., Buckley, D.A.H., et al.: Simultaneous optical polarimetry and X-ray observations of the magnetic CV CP TUC (AX J2315-592). MNRAS **306**, 809 (1999)
36. Ramsay, G., Potter, S., Cropper, M., et al.: Simultaneous optical polarimetry and X-ray data of the near-synchronous polar RX J2115-5840. MNRAS **316**, 225 (2000)
37. Romero-Colmenero, E., Potter, S.B., Buckley, D.A.H.: An eclipsing geometry for the polar QS Tel. ASPC **330**, 429, (2005)
38. Saxton, C.J., Wu, K.: Perturbative analysis of two-temperature radiative shocks with multiple cooling processes. MNRAS **310**, 677 (1999)
39. Saxton, C.J., Wu, K.: Stability analyses of two-temperature radiative shocks: formulation, eigenfunctions, luminosity response and boundary conditions. MNRAS **324**, 659 (2001)
40. Schwope, A.D., Beuermann, K., Jordan, S.: One-pole and two-pole X-ray emission in the AM Herculis binary BL HYI. A&A **223**, 179 (1989)
41. Smith, D.A., Dhillon, V.S.: The secondary stars in cataclysmic variables and low-mass X-ray binaries. MNRAS **301**, 767 (1998)
42. Warner, B.: Cataclysmic Variable Stars. Cambridge Astrophysics Series 28. Cambridge University Press, Cambridge (1995)
43. Watson, C.A., Dhillon, V.S.: Roche tomography of cataclysmic variables – I. artefacts and techniques. MNRAS **326**, 67 (2001)
44. Wickramasinghe, D.T., Meggitt, S.M.A.: The polarization properties of magnetic accretion columns. III – a grid of uniform temperature and shock front models. MNRAS **214**, 605 (1985)
45. Wickramasinghe, D.T., Ferrario, L.: Cyclotron emission from inhomogeneous shocks in AM Herculis-type systems. ApJ **334**, 412 (1988)
46. Woelk, U., Beuermann, K.: Stationary radiation hydrodynamics of accreting magnetic white dwarfs. A&A **306**, 232 (1996)
47. Wu, K.: Structure of inhomogeneous accretion shocks. Proc. Astron. Soc. Aust. **11**, 61 (1994)
48. Wu K.: Accretion onto magnetic white dwarfs. Space Sci. Rev **93**, 611 (2000)
49. Wu, K., Chanmugam, G.: Cyclotron spectra from inhomogeneous accretion columns. ApJ **331**, 861 (1988)

50. Wu, K., Chanmugam, G.: Cyclotron spectra from inhomogeneous accretion columns. II – polarization. ApJ **344**, 889 (1989)
51. Wu, K., Chanmugam, G.: Polarized cyclotron emission from three-dimensional accretion shocks. ApJ **354**, 625 (1990)
52. Wu, K., Chanmugam, G., Shaviv, G.: Structure of steady state accretion shocks with several cooling functions: closed integral-form solution. ApJ **426**, 664 (1994)
53. Wu, K., Wickramasinghe, D.T.: Three-dimensional structured shocks in Am-Herculis type systems – part one – the angular dependence of intensity and polarization from axisymmetric shocks. MNRAS **246**, 686 (1990)
54. Wu, K., Wickramasinghe, D.T.: Three-dimensional structured shocks in AM Herculis-type systems. II – cyclotron emission from ridge-shaped emission regions. MNRAS **256**, 329 (1992)